STRUCTURAL BIOLOGY

Amylum forms typical self-assembled amyloid fibrils

Sonika Chibh[1], Ashmeet Singh[2], Gal Finkelstein-Zuta[1,3], Gil Koren[4], Raya Sorkin[5,6], Roy Beck[4], Sigal Rencus-Lazar[1], Ehud Gazit[1,3]*

Amyloid fibril formation is a central biochemical process in pathology and physiology. Over decades, substantial advances were made in elucidating the mechanisms of amyloidogenesis, its links to disease, and the production of functional supramolecular structures. While the term "amyloid" denotes starch-like features of these assemblies, no evidence of amyloidogenic behavior of polysaccharides has been so far reported. Here, we investigate the potential of amylum (starch) not only to self-assemble into hierarchical fibrillar structures but also to exhibit canonical amyloidogenic properties. Ordered amylum structures were formed through a sigmoidal growth process with characteristic amyloid features including typical nanofibril morphology, binding to indicative dyes, inherent luminescence, apple-green birefringence upon Congo red staining, and notable mechanical rigidity. These findings shed light on polysaccharide self-assembly and expand the generic amyloid phenomenon.

INTRODUCTION

The amyloid fibril architecture constitutes the key supramolecular organization of aggregated proteins (*1*, *2*). While initially explored due to its role in human disorders (*3*, *4*), amyloid formation was found to be ubiquitous as disease-unrelated proteins form these remarkably thermodynamically stable nanostructures with typical biological, physical, and chemical properties (*5*–*7*). Amyloid fibril formation was also implicated in the physiology of a diverse group of organisms where the formation of functional amyloids was demonstrated (*8*–*10*). The unique physical properties of amyloid structures, including optics and mechanical characteristics, have been extensively studied for technological applications (*11*–*13*).

Historically, in 1854, the term "amyloid" was derived from the Latin word amylum and the Greek word amylon, which describes starch stained with iodine (*14*). A few years later, in 1859, Friedrich and Kekule identified amyloid as mainly composed of protein and a small amount of glycosaminoglycan (GAG) (*15*, *16*). For over a century, carbohydrates have been known to be associated with the deposition of amyloids (*17*). However, no direct evidence of amyloid formation by carbohydrates has been reported until the mid-20th century. A clinical study published in 1966 revealed that amyloid material took up some stains, suggesting the presence of mucopolysaccharides (*18*). In 1990, another study showed in vivo association between cardiac amyloid fibrils and GAGs (*19*). Further in 2008, a study demonstrated that endogenous polysaccharides promoted fibrillar structures of amyloid-β(1-42) (*20*).

In 2011, another study showed that carbohydrates, in particular GAG, have scaffold-like properties that accelerate in vitro amyloidogenesis (*21*). Recently in 2021, a study showed that polysaccharides such as glycogen, phytoglycogen, mannan, and cinnamoyl-modified glycogen were found to accelerate fibril formation (*22*). Furthermore, studies have also shown that the brains of patients with Alzheimer's disease contain lipopolysaccharides within the amyloid deposits (*23*, *24*).

The role of polysaccharides in amyloid formation is very intriguing as these polymers are the most abundant biomolecules, making up ~80% of the biomass on Earth (*25*). Yet, there has been no report regarding their potential amyloid behavior. This lack of knowledge is particularly remarkable, as it is well-known in the literature that polysaccharides such as cellulose (*26*), chitin (*27*), and inulin (*28*) have a strong propensity to self-assemble into well-defined structures with notable physiochemical properties. In addition, Congo red (CR), an amyloid-specific dye, has shown birefringence upon binding to carbohydrates, suggesting a possible amyloid-like structural orientation of these molecules in their aggregated state (*29*). Despite this evidence on polysaccharide-based self-assembled structures, no experimental observation of polysaccharide-based amyloid fibrils has been reported so far.

In light of this, here, we aimed to explore the ability of starch to self-assemble and form typical amyloid-like fibrils. For this purpose, we investigated whether starch can produce fibrils with typical amyloid characteristics, including amyloid-specific dye binding (*30*), inhibition of fibril growth by polyphenols (*31*), autofluorescence (*32*), apple-green birefringence (*29*), mechanical stiffness (*33*), and piezoelectric properties (*34*). While the mechanism of amyloid formation by starch is not yet fully understood, this study provides a proof of concept for a deeper understanding of the role of polysaccharides in amyloidogenesis. In addition, the important mechanistic insights aligned with the pathology of age-related neurodegenerative disorders, this work substantially extends the generic amyloid hypothesis to provide a fundamental understanding of both the amyloid phenomenon and its implications in pathology, physiology, and nanotechnology.

RESULTS

Self-assembly of starch into amyloid-like fibrils

We first examined whether starch could self-assemble into ordered structures with amyloid-like characteristics. For this purpose, starch powder was dissolved in phosphate-buffered saline (1× PBS, pH 7.4) at different concentrations (0.0156, 0.03125, 0.0625, 0.125, 0.25, 0.5,

[1]The Shmunis School of Biomedicine and Cancer Research, George S. Wise Faculty of Life Sciences, Tel Aviv University, Tel Aviv 6997801, Israel. [2]Center for Biotechnology and Interdisciplinary Studies (CBIS), Rensselaer Polytechnic Institute, Troy, NY 12180, USA. [3]Department of Materials Science and Engineering, Iby and Aladar Fleischman Faculty of Engineering, Tel Aviv University, Tel Aviv 6997801, Israel. [4]The Raymond & Beverly Sackler School of Physics and Astronomy, The Center for Nanoscience and Nanotechnology, and the Center for Physics and Chemistry of Living Systems, Tel Aviv University, Tel Aviv 69978, Israel. [5]School of Chemistry, Raymond & Beverly Sackler Faculty of Exact Sciences, Tel Aviv University; Tel Aviv, 6997801, Israel. [6]Center of Physics and Chemistry of Living Systems, Tel Aviv University; Tel Aviv, 6997801, Israel.
*Corresponding author. Email: ehudg@post.tau.ac.il

and 1 mg/ml), which was then heated to 90°C for 5 hours, followed by gradual cooling down to room temperature to allow for self-assembly (Fig. 1A).

Various microscopy techniques were used to assess the presence of organized structures and examine their morphology. Initially, transmission electron microscopy (TEM) was used to examine the impact of the starch concentration on the formation of self-assembled structures (Fig. 1, B to H). Notably, it was observed that the 0.01-, 0.025-, 0.05-, 0.1-, and 0.25-mg/ml solutions (Fig. 1, B to F, respectively) did not exhibit any notable ordered nanostructure; however, at 0.5 and 1 mg/ml, we observed well-organized and elongated amyloid-like fibrils (Fig. 1, G and H). We further investigated this morphology in detail since we observed amyloid-like fibrils at the concentration of 0.5 mg/ml.

Once the fibers were formed at 0.5 mg/ml concentration of starch, they were quite robust in nature. They persisted the fibrillar structure even after prolong heating at 90°C. The TEM micrographs for the postheated fibers strongly supported its thermodynamic stability that aligns with one of the characteristic feature of amyloid fibrils (fig. S1).

Further by analyzing the nanofibrils (Fig. 1I) in various TEM micrographs, the mean diameter was calculated to be 15.371 ± 3.451 nm, and the length was found to range in micrometers as shown in Fig. 1J. In addition, when the self-assembled solution was imaged using atomic force microscopy (AFM), micrographs affirmed the formation of elongated nanofibrils (Fig. 1K), consistent with the TEM observations, with an average height of ~11.5 nm (Fig. 1L).

In addition, small-angle x-ray scattering (SAXS) patterns of the starch fibrils were recorded. SAXS data revealed distinct characteristics of the fibrils when recorded in a q range of 0.004 to 0.16 $Å^{-1}$ (Fig. 1M). The fibrils displayed a pronounced peak in the lower q range and were well-fitted in a long cylinder model via Porod approximation, indicating a diameter of ~14.66 nm, consistent with the diameter deduced from TEM imaging (*35*, *36*). To further characterize the presence of functional groups, Fourier transform infrared (FTIR) spectroscopy was used showing varying stretching vibrations of starch fibrils. The broad peak at 3452 cm^{-1} corresponding to O—H was attributed to the stretching vibration of H_2O. However, the peak at 1630 cm^{-1} was associated with the first overtone of —OH bending or H_2O deformation. Further, the band at 1083 cm^{-1} corresponded to the —C—O symmetric stretching vibration (Fig. 1N) (*37*).

We further set out to investigate if self-assembled nanofibril growth exhibited a sigmoidal curve, a characteristic of amyloid fibrils (*38*). For this purpose, a turbidity assay at a wavelength of 350 nm was performed to determine the kinetics of fibril formation. Starch nanofibril formation followed a sigmoidal growth pattern in the same manner as amyloid fibrils (Fig. 1O) (*38*). Using same kinetics growth curve assay, the conversion rate of starch from monomers to fibrils was calculated. It was observed that the conversion rate was highest at 0.5-mg/ml starch concentration in comparison to 0.25- and 1-mg/ml concentrations (table S1).

Another distinctive property associated with amyloid fibrils is intrinsic fluorescence in the blue-green region, irrespective of the presence of any aromatic moieties in the molecule, upon excitation at wavelengths higher than 350 nm (*32*, *39*). To gain insight into the starch nanofibril fluorescence property, we initially recorded the fluorescence spectra of starch nanofibrils at an excitation wavelength ranging from 350 to 400 nm. The spectra indicated a broad and characteristic emission peak in the range of 400 to 550 nm, showing increased intensity as the excitation wavelength increased. This enhanced intensity was directly related to the blue-green intrinsic fluorescence of the fibrils as shown in Fig. 1P. As an additional confirmation of the autofluorescence property of starch fibrils, the sample was excited under ultraviolet (UV) light (λ_{max}, 365 nm), demonstrating a distinct blue-green color when compared to only PBS (Fig. 1Q).

Next, we sought to ascertain whether the starch fibrils showed an ordered packing or arrangement, a characteristic amyloid fibrils property. Amyloid fibrils are known to display a typical apple-green birefringence upon binding to the CR dye in an ordered fashion under polarized light (*29*). To assess the amyloidogenicity of the starch nanofibrils, fibrils were stained with CR dye and visualized under a cross-polarized microscope (Fig. 2, A to D) (*29*, *40*). We observed the emergence of apple-green birefringence when CR-stained fibrils were imaged under cross-polarized light, similar to the birefringence observed for amyloid fibrils (Fig. 2, A and B). In a control experiment, when native CR dye was examined, no birefringence was detected (Fig. 2, C and D).

Next, we tested whether starch nanofibrils could bind to another amyloid-specific dye, Thioflavin T (ThT). When bound to amyloid fibrils, ThT emits a characteristic emission peak at 485 nm upon excitation at 420 nm (*41*). Therefore, this fluorometric approach allowed us to determine the kinetics of amyloid formation (*42*). The results of ThT fluorescence kinetics assay showed a sigmoidal growth curve, where the lag phase was followed by the elongation phase and subsequently a plateau (Fig. 2E). ThT-stained fibrils were further analyzed using confocal microscopy. ThT-stained fibrils showed green fluorescence, confirming their amyloidogenic nature (Fig. 2F).

We further examined the effect of (−)-epigallocatechin gallate (EGCG), a polyphenol known to inhibit amyloid fibril formation (*31*). First, the dose-dependent effect of EGCG was examined using TEM (Fig. 2, G to I). At 0.25 mM EGCG, a few fibril-like aggregates (Fig. 2H) were observed, whereas at 0.5 mM EGCG, starch did not exhibit any detectable self-assembly (Fig. 2I).

Moreover, we assessed how EGCG affected starch amyloid formation kinetics by measuring turbidity (Fig. 2J). The addition of EGCG solution (0.5 mM) led to a notable inhibitory effect which completely prevented the formation of starch nanofibril. Conversely, when a twofold-diluted concentration of EGCG (0.25 mM) was used, only a few fibrils were observed and the absorbance was reduced by ~50% compared to fibrils alone as shown in Fig. 2J.

Second, the assay was conducted using a ThT-based fluorescent dye to assess the effect of EGCG on starch assemblies (Fig. 2K). The ThT assay also demonstrated complete inhibition of fibril formation at an EGCG concentration of 0.5 mM. It was observed that EGCG caused ~40% reduction in ThT intensity at an EGCG concentration of 0.25 mM when compared to native fibrils (Fig. 2K). These results suggested that at a lower EGCG concentration, starch fibrils were notably reduced, whereas, at a higher concentration, complete inhibition of intensity was observed.

Further, additional FTIR spectra were recorded to examine the effect of EGCG on the functional groups of starch fibrils. The two spectral graphs presented in Fig. 2 (L and M) displayed noticeable differences mainly in the peak regions of C—O and —OH groups, suggesting that EGCG has disrupted the fibril morphology. It is

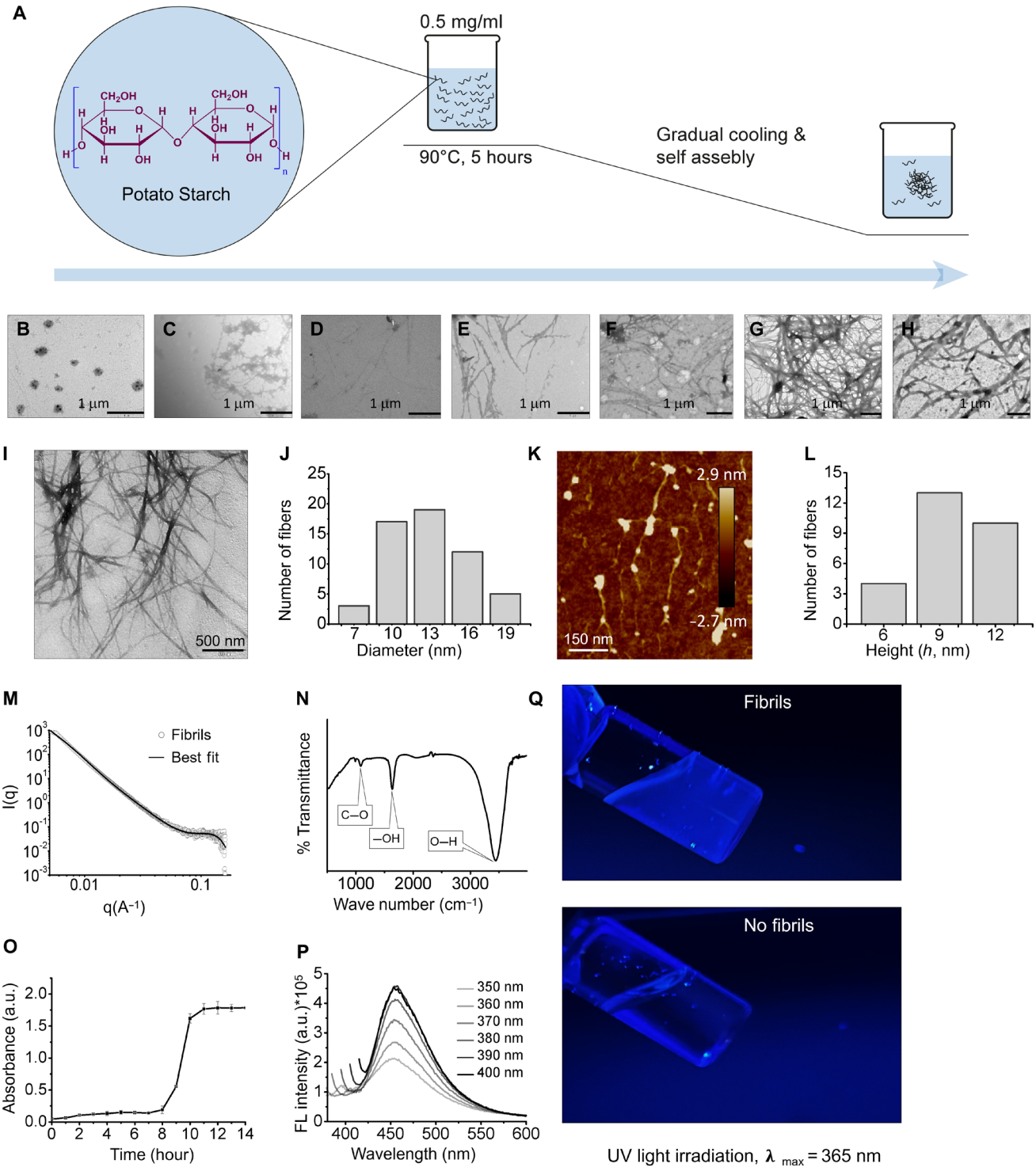

Fig. 1. Formation of amyloid like fibrils by starch self-assembly. (**A**) A schematic depiction illustrating the formation of starch fibrils. Fibrils were formed in PBS (pH 7.4) after heating the starch solution to 90°C for 5 hours and gradually cooling it to room temperature. (**B** to **H**) TEM images of starch assemblies formed at different concentrations. (B) 0.0156, (C) 0.03125. (D) 0.0625, (E) 0.125, (F) 0.25, (G) 0.5, and (H) 1 mg/ml. Scale bars, 1 µm. (**I**) TEM image of 10× diluted starch fibrils formed at a concentration of 0.5 mg/ml. (**J**) Diameter distribution profile of the fibrils. (**K**) AFM tapping mode analysis of 10x diluted starch fibrils formed at a concentration of 0.5 mg/ml (**L**) showing the formation of elongated fibrils with an average height of ~11.5 nm. (**M**) A SAXS profile of starch fibrils formed at a concentration of 0.5 mg/ml. (**N**) FTIR spectrum of starch fibrils formed at a concentration of 0.5 mg/ml. (**O**) A turbidity assay at 350 nm illustrating starch fibrillation growth in a sigmoidal pattern. (**P**) Fluorescence spectroscopy analysis at an excitation wavelength range of 350 to 400 nm. (**Q**) Images recorded under UV light (λ_{max} = 365 nm) of a glass vial containing starch fibrils compared to PBS as a control.

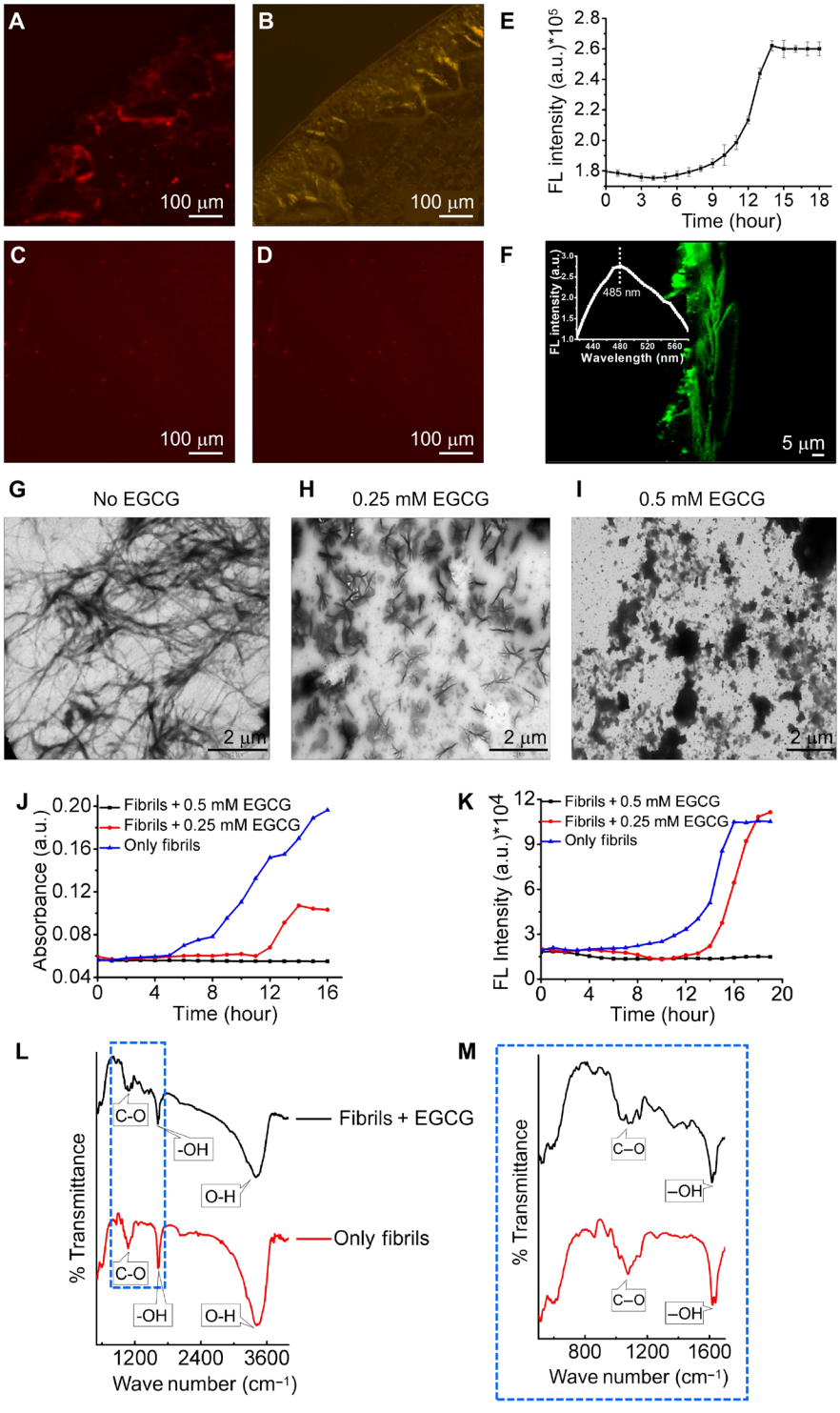

Fig. 2. Starch fibrils exhibit amyloid like characteristics. (**A**) CR-stained starch fibrils (left) under non-polarized light and (**B**) under cross-polarized light. (**C**) CR only as a control under non-polarized light and (**D**) under cross-polarized light. (**E**) Starch fibrils subjected to a ThT binding assay. ThT was added to the starch solution at a concentration of 20 μM, and the fluorescence spectra were recorded at 420-nm excitation and 485-nm emission. (**F**) Confocal microscopy of the ThT-stained starch fibrils. Inset: The fluorescence spectrum recorded from confocal microscopy. (**G** to **I**) TEM images of starch (G) in the absence of EGCG, (H) 0.5 mM, and (I) 0.25 mM EGCG. (**J**) Turbidity assays of starch in the presence of 0.25 and 0.5 mM EGCG. Starch without EGCG served as a control. (**K**) ThT binding assays of starch in the presence of 0.25 and 0.5 mM EGCG. Starch without EGCG served as a control. (**L**) FTIR analysis of the starch fibrils. (**M**) Zoomed FTIR peaks.

worth noting that the C—O and —OH bands were previously reported to be sensitive to changes in the starch structure (*37*). The peaks at a wave number of ~911 and 1081 cm^{-1} were attributed to the presence of the C—O group, but after the addition of EGCG, the peaks in the 900 to 1600 cm^{-1} region were altered, whereas some new peaks also appeared. After EGCG was added to starch in its self-assembled fibril state, a change in vibrations of functional groups confirmed that the fibrils' morphology had been disturbed.

Detailed morphology of starch fibrils using MATLAB FiberApp application

To provide a more detailed characterization of starch fibrils morphology, an advanced analysis was conducted using a MATLAB FiberApp application. The analysis involved the comprehensive examination of height distribution profiles, length distribution profiles, persistence length, scaling behavior, and orientation of fibrils using both AFM and TEM images (*43*). First, the AFM image (Fig. 3A) was flattened (Fig. 3B) using polynomial functions, which

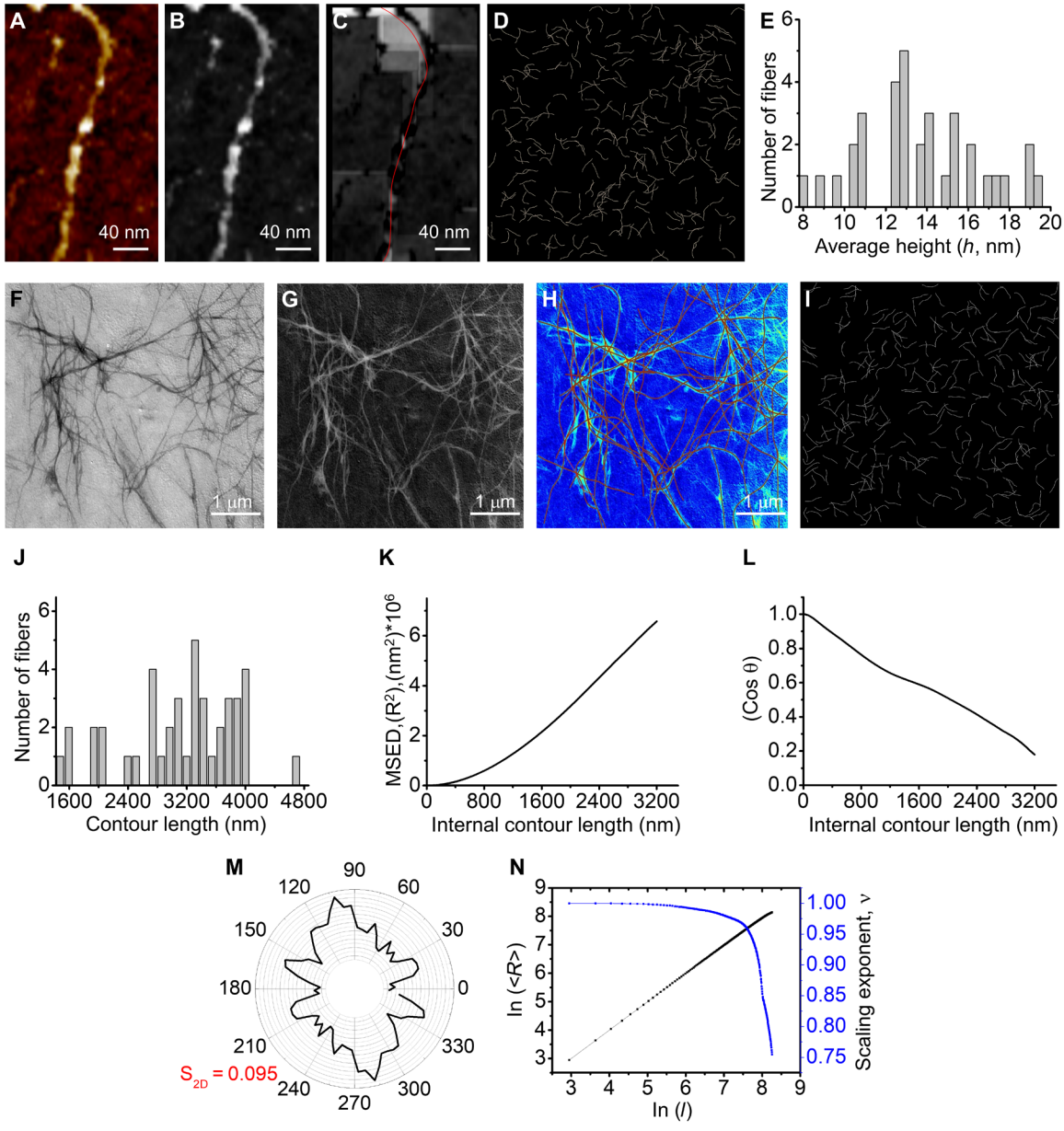

Fig. 3. MATLAB analysis of starch fibrils. (**A**) AFM image of the starch fibril. (**B**) AFM image after uneven background illumination. (**C**) Active tracking of a fiber, represented in red color. (**D**) Simulated image of the contours generated using fiber/image generator. (**E**) Fibril height distribution profile showing an average height of 12.15 nm. (**F**) TEM image of the starch fibrils. (**G**) An image generated using MATLAB software after uneven background illumination. (**H**) TEM colormap image showing the tracking of fibrils. (**I**) Simulated image of the contours generated using fiber/image generator. (**J**) Fibril length distribution profile with an average contour length of 3198.80 nm. (**K**) MSED with internal contour length was used to calculate a persistence length of 1223.46 ± 16 nm for the starch fibrils. (**L**) The persistence length of starch fibrils was calculated as 1427.52 ± 21 nm using BCF. (**M**) An orientation distribution of contour segments of fibrils shows random orientations. (**N**) An average natural log of end-to-end distance along with the natural log of internal contour length profile and scaling exponent propagation for starch fibrils indicate a flexible nature.

corrected the background of the image. As a result, the "Set Zero Level" procedure was used to correct uneven illumination of the AFM image (Fig. 3B) with high accuracy. This method facilitated the calculation of the root mean square value of surface roughness during the tracking of fibrils. After uneven illumination of the background, tracking of fibrils was performed using the A* pathfinding algorithm provided in the software (Fig. 3C). Then, a simulated image of the fibrils was created using a fiber/image generator (Fig. 3D). After optimizing all image parameters, the height profile of the starch fibrils was determined. On the basis of MATLAB analysis, the fibrils exhibited an average height of 12.26 nm (Fig. 3E). The average height results obtained using MATLAB software were in agreement with the results obtained from AFM line analysis.

Subsequently, further MATLAB analysis of fibrils was performed using a TEM image (Fig. 3F). Following the protocol outlined above, the background of the TEM image was corrected as Set Zero Level (Fig. 3G). Then, tracking of fibrils was performed using the A* pathfinding algorithm provided in the software. Figure 3H presents the TEM image with tracked fibrils in jet colormap. The simulated image of the contours was generated using fiber/image generator parameters from the corresponding TEM image (Fig. 3I).

In addition to the extensive analysis of starch-based self-assembled fibrils, we further calculated the persistence length of the starch nanofibrils, another important characteristic feature of amyloid fibrils to analyze their mechanical properties. For this purpose, we first analyzed the length distribution profile along with the contour length of the fibrils to estimate their persistence length. As shown in Fig. 3J, the estimated average contour length of the fibrils was 3198.80 nm. Subsequently, we calculated the persistence length of the fibrils using mean square end-to-end distance (MSED) and bond correlation function (BCF). Using either approach, the persistence length of the fibrils was calculated to be 1223.46 ± 16 nm (Fig. 3K) and 1427.54 ± 21 nm (Fig. 3L), respectively. In either case, the contour length exceeded the calculated persistence length, indicating the flexible nature of the starch-based self-assembled fibrils.

An orientation of fibers contributes to stiffness and strength properties, which are crucial for mechanical performance (*44*). To measure fibril alignment properties, the orientation distribution was calculated. Fig. 3M illustrates a random orientation of fibrils distributed in every direction. In addition, the two-dimensional (2D) order orientation parameter was calculated using equation $S_{2D} = \langle 2\cos^2\theta - 1\rangle$ for fibrils, where θ is defined as the angle between the *n*th segment and the local director in the chosen area. As reported, a perfect orientation order is indicated when the value of the 2D order parameter approaches 0.99 (*45*). On the basis of our analysis, we calculated the starch fibrils' 2D order orientation (S_{2D}) parameter to be 0.095, indicating that fibrils were randomly oriented (*45*). In addition, the scaling exponent which is the average MSED as a power law function of the internal contour length (l) was estimated for the starch fibrils. The scaling exponent approaches 1 when the internal contour length is smaller than the persistence length ($l < \lambda$). However, when the internal contour length is higher than the persistence length ($l > \lambda$), the scaling exponent is 0.75 in 2D, which reflects the flexible nature of fibrils (*46*). Hence, the linear fit of the natural log of MSED versus the natural log of contour length was calculated, resulting in a scaling exponent value of 0.75 (Fig. 3N), confirming the flexible nature of the fibers.

Mechanical stiffness studies of starch fibrils

To gain insights into the mechanical stiffness of starch fibrils, AFM-based nanoindentation experiments were performed to assess their potential as mechanical device materials (Fig. 4A). PeakForce QNM mode, which consists of Peak Force Tapping mode, was used to conduct a quantitative nanomechanical analysis of the fibrils based on individual force versus separation curves, allowing to map the material properties (*47*). The results were presented in different modes of imaging such as height image, 3D height image, peak force, Derjaguin-Muller-Toporov (DMT) modulus, adhesion, indentation, and deformation images (Fig. 4, B to H, respectively). To measure the mechanical properties of the starch fibrils, the tip was placed in the middle of a fiber surface, and force-distance curves were recorded at that same position. Figure 4I shows a force-distance curve for a fiber along with the corresponding cantilever deflection curve. The measured elasticity of the starch fibrils showed Young's modulus value of 6.729 GPa (Fig. 4J), in agreement with the range of 3 to 20 GPa previously reported for typical amyloids (*12*). Each datapoint of the modulus image was represented by a histogram showing the modulus values. The histogram shown in Fig. 4J illustrates the distribution of stiffness values at each data point recorded. Further, the average point stiffness values derived from the curves were plotted as a function of the measurement counts (Fig. 4K). The histogram indicated the stiffness values of 100 datasets recorded on fiber in the peak force image (Fig. 4L).

Characterization of a starch-based nanogenerator

Last, we aimed to further evaluate the piezoelectric properties of starch fibrils (Fig. 5A). Since piezoelectricity is defined as the linear conversion of mechanical energy into electrical energy, it can be easily evaluated by measuring the voltage generated in response to force application. Together with the voltage and force signals, the piezoelectric assessment can be described by the linear graph of the voltage generated correlated to the force applied, as a proof of concept for the fabrication of a nanogenerator. The starch fibrils were tested for their ability to generate electrical power by a custom-designed setup upon applying mechanical force. As shown in Fig. 5 (B and C), the output voltage generated by the active layer of the starch assemblies increased linearly when increasing the applied force, indicating that piezoelectricity was the origin of the generated voltage. The assemblies could generate 100 mV voltage upon application of 25 N force, confirming the piezoelectric nature of the material.

DISCUSSION

In summary, we describe the concentration-dependent self-assembly of starch into amyloid-like fibrils. Starch molecules consist of linear or branched glucosyl units, each containing three hydroxyl groups that readily form intermolecular and intramolecular hydrogen bonds. These interactions cause starch to form amyloid-like fibrils when it is gradually cooled to room temperature. It is well established that hydrogen bonding could be notably important in the stability of polysaccharide structures such cellulose (*48*), and we assume that this is also the case in this unique supramolecular arrangement of these building blocks. This work suggests/entails a substantial extension to the generic amyloid hypothesis and provides mechanistic insights into this newly described phenomenon.

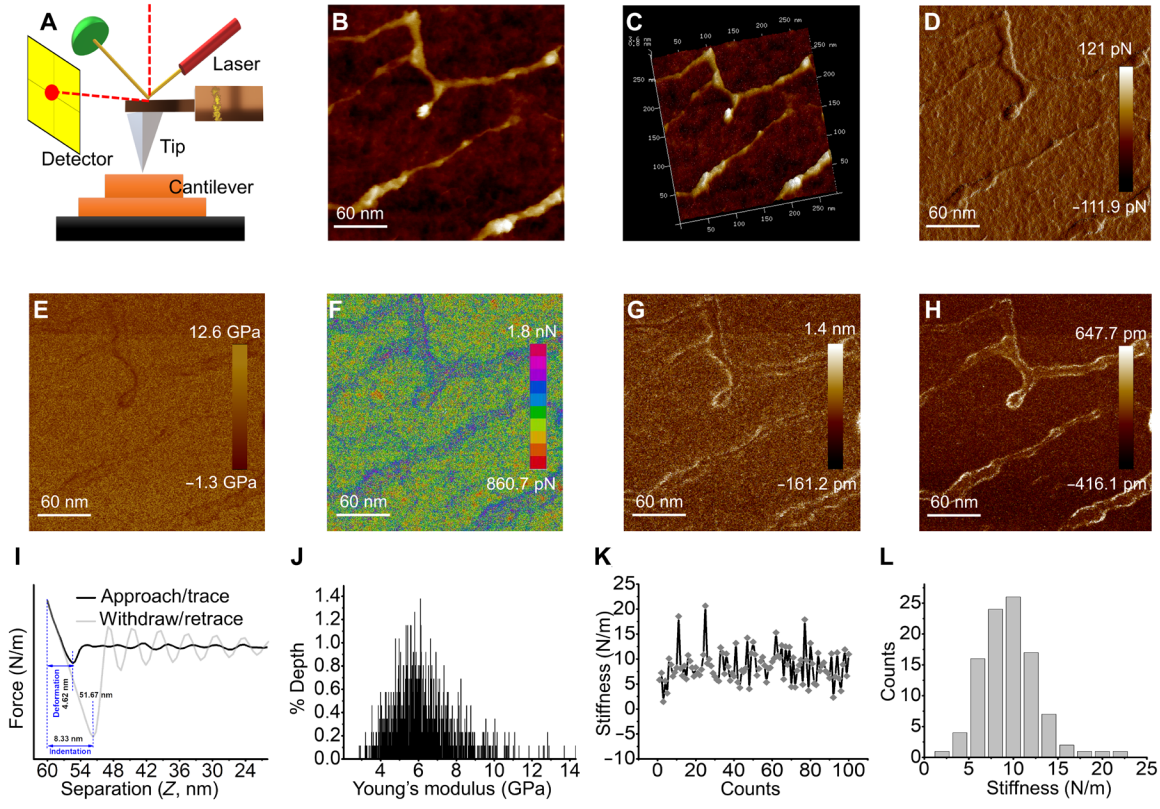

Fig. 4. Mechanical properties of starch fibrils. (**A**) Schematic representation of AFM indentation experiments performed on starch fibrils. (**B** to **H**) AFM images of starch fibrils were captured in different modes. (B) Height image. (C) 3D Height image. (D) PeakForce image. (E) DMT modulus image. (F) Adhesion image. (G) Indentation image. (H) Deformation image. (**I**) A typical force-displacement curve based on the DMT model. (**J**) Histogram showing the distribution of measured Young's modulus of starch fibrils. The average Young's modulus was calculated as 6.729 GPa. (**K**) Fibril stiffness values were derived from 100 individual measurements obtained in a single experiment versus measurement number (count). (**L**) Histogram of the stiffness distribution of starch fibrils. The average stiffness derived from all measurements was calculated as 9.6 N/m.

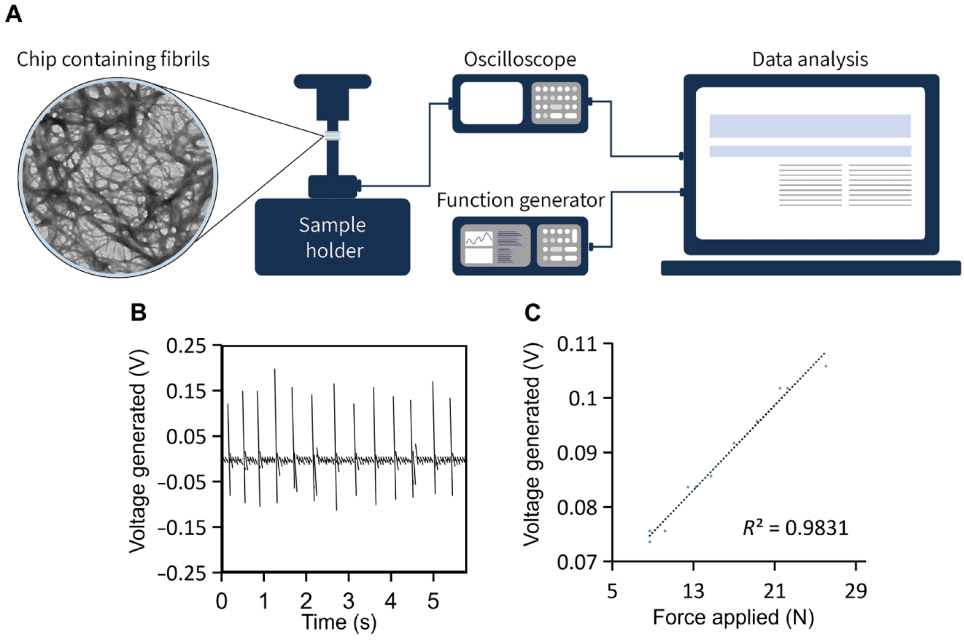

Fig. 5. Piezoelectric properties of starch fibrils. (**A**) Schematic representation of the experimental setup used to determine the piezoelectric properties of starch fibrils. A piezoelectric actuator, oscilloscope, and function generator make up the device setup. Fibrils containing piezoelectric layers were mechanically force-tested and monitored by force sensors. (**B**) A graph displaying the open circuit voltage generated by force application over time. (**C**) A linear correlation between the voltage generated and the applied force.

Previous studies have identified the ability of various building blocks to form amyloid-like fibrils. Yet, this study describes the formation of starch fibrils that display a typical fibrillar morphology, ThT fluorescence binding profile, birefringence, autofluorescence, and reduced fibril formation in the presence of EGCG. In addition, the newly identified structures also exhibit mechanical stiffness and piezoelectric properties, additional features that were identified for proteinaceous and nonproteinaceous amyloids (*12*, *34*, *49*, *50*).

Amyloid deposits have been associated with various diseases (*4*) for more than a century but in addition to their clinical relevance, these supramolecular entities can also play an important role in physiology and technology. Amyloid fibril formation has been physiologically implicated in a diverse group of organisms ranging from bacteria to humans for the formation of functional amyloids (*9*, *51*), and a large number of technological applications have also been developed based on the unique physical properties of amyloid structures, including optics (*11*, *52*), electronics (*53*), mechanics (*33*, *54*, *55*), and internal medicine (*56*).

Polysaccharide-based fibrous materials are becoming more popular in biomedical research due to their mechanical strength, porosity, surface area–to–volume ratio, and tunability. These fibrils could entangle with each other to form dispersion with a certain viscosity with a higher water-holding capacity. These can be used as a tissue regenerative stimulator in patients with knee wounds where their movement will not be restricted and the dressing will not fail. These polysaccharide-based fibrils are particularly beneficial in preventing degradation of drugs and avoiding drawbacks such as poor solubility in water and a short half-life (*57*, *58*). Therefore, these starch-based fibrils could be more stable, reusable, and denature resistant than nucleic acids and proteins. Therefore, the current work has many far-reaching implications for numerous aspects of pathology, physiology, and technology.

MATERIALS AND METHODS

Preparation of starch assemblies

A heat-cool method was used to prepare the starch assemblies. Potato starch (Sigma-Aldrich) was dissolved in PBS (pH 7.4) at the following concentrations: 0.0156, 0.03125, 0.0625, 0.125, 0.25, 0.5, and 1 mg/ml. To obtain self-assembled structures, solutions were heated to 90°C for 5 hours and gradually cooled to room temperature. Further the thermal stability of these preformed fibrils was analyzed using TEM after prolong heating at 90°C.

Transmission electron microscopy

A 6-μl sample of starch solution of various concentrations was drop-casted on a copper grid with a 400 mesh. The excess fluid was removed with Whatman filter paper after 15 min. The grid was then dried in a desiccator under vacuum. A JEOL 1200EX electron microscope was used to image samples at 80 kV.

Atomic force microscopy

A 10-μl sample of a starch solution at a concentration of 0.5 mg/ml was cast onto a freshly prepared silicon wafer. The sample was allowed to dry at room temperature. A PeakForce tapping mode with ScanAsyst (Bruker's Dimension ICON AFM) was used to capture images.

Confocal microscopy

ThT (20 μM) dye was used to stain fibrils prepared at a starch concentration of 0.5 mg/ml in PBS pH 7.4. A stained sample was drop-casted on a glass slide and covered with a cover slip. A Carl Zeiss Jena, inverted LSM 510 META confocal laser scanning microscope was used to capture images at an excitation wavelength of 458 nm and an emission range of 480 to 595 nm.

Small-angle x-ray scattering

The scattering pattern of starch fibrils at a concentration of 0.5 mg/ml was measured in 1.5-mm quartz capillary. SAXS measurement was performed in the q range of 0.004 to 0.16 $Å^{-1}$ using an x-ray scattering system, with a GeniX (Xenocs) low-divergence Cu Kα radiation source (wavelength of 1.54 Å) and a scatterless slits setup. 2D scattering data were collected at a sample-to-detector distance of ~230 mm on a Pilatus 300 K detector (Dectris) and radially integrated using MATLAB (MathWorks)–based procedures (SAXSi). To obtain background scattering data, the buffer solution alone was measured. After subtracting the background from the sample, the scattering correlation peak was fitted using a long cylinder model with the Porod approximation.

Fluorescence spectroscopy

A 1-ml solution of starch fibrils was transferred into a quartz cuvette of 1 cm path length, and the spectrum was recorded using Horiba, Kyoto, Japan, FluoroMax-4 Spectrofluorometer at ambient temperature. Excitation and emission wavelengths ranged from 350 to 400 nm and 400 to 600 nm, respectively.

Turbidity assay

Starch (0.5 mg/ml) in PBS was heated to 90°C for 5 hours and immediately transferred to a 96-well flat bottom transparent plate (Corning) for turbidity measurement. The data were recorded at 350 nm using CLARIOstar BMG LABTECH microplate reader.

Conversion rate of monomers to fibrils

Starch (0.25, 0.5, and 1 mg/ml) was heated to 90°C for 5 hours and immediately transferred to a 96-well flat bottom transparent plate (Corning) for turbidity measurement. The data were recorded at 350 nm using CLARIOstar BMG LABTECH microplate reader.

ThT fluorescence kinetics assay

Starch solution at a concentration of 0.5 mg/ml heated to 90°C was mixed with 20 μM ThT and transferred to a 96-well black plate. Starch fibrils growth was monitored at 420 and 485 nm excitation and emission wavelengths, respectively. Data were collected using CLARIOstar BMG LABTECH microplate reader.

CR birefringence

Eighty-percent aqueous ethanol was used to prepare a saturated CR solution. A mixture of 5 μl of starch fibrils and 5 μl of CR dye solution was incubated for 10 min and drop-casted onto a glass side followed by room temperature drying. A Nikon DS Ri1 digital camera was used to take digital images under a Nikon Eclipse TI polarizing microscope.

Effect of EGCG on starch fibrils

A starch solution at a concentration of 0.5 mg/ml was dissolved in PBS for 5 hours at 90°C. The solution was then mixed with EGCG at

either 0.25 or 0.5 mM. TEM was used to analyze the morphology of the assemblies. Furthermore, a turbidity assay was performed as outlined above, in the presence or absence of EGCG.

In addition, the kinetics of ThT were examined after the addition of EGCG. Similarly, starch was dissolved in PBS at 90°C for 5 hours at a concentration of 0.5 mg/ml. Inhibitor EGCG was mixed with the solution at two different concentrations of 0.25 mM and 0.5 mM. At 420-nm excitation and 485-nm emission, a CLARIOstar BMG LABTECH microplate reader was used to determine the change in fluorescence with time after adding ThT (20 μM).

FTIR spectroscopy

Starch solution at a concentration of 0.5 mg/ml in PBS was heated to 90°C for 5 hours. EGCG was added to the solution at a concentration of 0.5 mM. The sample was dropped onto the IR-card and allowed to dry at room temperature for 100 μl. The IF spectra were recorded using a Nicolet 6700 FTIR spectrometer (Thermo Fisher Scientific, Waltham, Massachusetts, USA) from 4000 to 400 cm^{-1} at room temperature.

Fibril tracking and analysis using the FiberApp software

The in-house MATLAB FiberApp application was used to analyze the morphology of starch fibrils in detail. An uneven background from microscopy images was illuminated using polynomial surface flattening. As a result, the "remove surface processing" and "set zero level" functions were used to correct the background of the images. Using a set of coordinates, fibrils were tracked in the form of a contour, and their position was estimated.

Each contour's initial position was calculated using the A* pathfinding algorithm. AFM and TEM images with a resolution of 5120 × 5120 pixels were used to extract data from traced fibrils. Using the software, different characteristic features such as length distribution, persistence length, orientation distribution, and scaling exponent were determined. In-house software was used for data processing and analysis.

Mechanical analysis

All AFM experiments were carried out using a Bruker's Dimension ICON AFM equipped with a closed loop scanner. Images of starch fibrils were obtained in AFM tapping mode. To measure the mechanical properties of the starch fibrils, an indentation experiment was performed, with the microscope employed in force curve mode, and the deflection (force) of the cantilever plotted as a function of sample height. The cantilevers used in these experiments (RTESPA-300 probe) had a tip radius of 5 to 10 nm, k ~ 42 N/m, which allowed to apply the relatively high loads required to indent the starch fibrils. The measured point stiffness was mathematically derived from the slope of the linear force-distance curve.

Piezoelectric nanogenerator fabrication

The nanogenerator was fabricated in a sandwiched configuration. Flexible polyethylene terephthalate coated with a thin layer of indium tin oxide (ITO) were used as the top and bottom electrodes, respectively, allowing the measurement of an open circuit voltage. In between the electrodes, a thin layer of ultrathin Kapton tape with a circular vacancy (5 mm in diameter) was applied to avoid a short circuit. The starch fibrils were deposited in the interior part of the Kapton tape, atop the ITO-coated electrode.

Electromechanical measurements

The piezoelectric effect was evaluated using a simple costume-built setup designed to perform electromechanical measurements of the voltage generated by a piezoelectric sample in response to force application. Force was applied by drop weight impact test, while the magnitude of the force was monitored by a (PCB Piezotronics, 208C02). The output voltage signals of the sample and the force signals were acquired using a digital oscilloscope (Keysight EDUX1002A).

Supplementary Materials

This PDF file includes:

Table S1
Fig. S1

REFERENCES AND NOTES

1. L. Gremer, D. Schölzel, C. Schenk, E. Reinartz, J. Labahn, R. B. G. Ravelli, M. Tusche, C. Lopez-Iglesias, W. Hoyer, H. Heise, D. Willbold, G. F. Schröder, Fibril structure of amyloid-β(1–42) by cryo–electron microscopy. *Science* **358**, 116–119 (2017).
2. D. Willbold, B. Strodel, G. F. Schröder, W. Hoyer, H. Heise, Amyloid-type protein aggregation and prion-like properties of amyloids. *Chem. Rev.* **121**, 8285–8307 (2021).
3. A. Aguzzi, C. Haass, Games played by rogue proteins in prion disorders and Alzheimer's disease. *Science* **302**, 814–818 (2003).
4. D. Eisenberg, M. Jucker, The amyloid state of proteins in human diseases. *Cell* **148**, 1188–1203 (2012).
5. E. Gazit, The "correctly folded" state of proteins: Is it a metastable state? *Angew. Chem. Int. Ed. Engl.* **41**, 257–259 (2002).
6. A. J. Baldwin, T. P. J. Knowles, G. G. Tartaglia, A. W. Fitzpatrick, G. L. Devlin, S. L. Shammas, C. A. Waudby, M. F. Mossuto, S. Meehan, S. L. Gras, J. Christodoulou, S. J. Anthony-Cahill, P. D. Barker, M. Vendruscolo, C. M. Dobson, Metastability of native proteins and the phenomenon of amyloid formation. *J. Am. Chem. Soc.* **133**, 14160–14163 (2011).
7. A. K. Buell, Stability matters, too—The thermodynamics of amyloid fibril formation. *Chem. Sci.* **13**, 10177–10192 (2022).
8. R. Hervas, M. J. Rau, Y. Park, W. Zhang, A. G. Murzin, J. A. J. Fitzpatrick, S. H. W. Scheres, K. Si, Cryo-EM structure of a neuronal functional amyloid implicated in memory persistence in *Drosophila*. *Science* **367**, 1230–1234 (2020).
9. S. A. Levkovich, E. Gazit, D. Laor Bar-Yosef, Two decades of studying functional amyloids in microorganisms. *Trends Microbiol.* **29**, 251–265 (2021).
10. M. R. Chapman, L. S. Robinson, J. S. Pinkner, R. Roth, J. Heuser, M. Hammar, S. Normark, S. J. Hultgren, Role of *Escherichia coli* curli operons in directing amyloid fiber formation. *Science* **295**, 851–855 (2002).
11. L. Grisanti, M. Sapunar, A. Hassanali, N. Došlić, Toward understanding optical properties of amyloids: A reaction path and nonadiabatic dynamics study. *J. Am. Chem. Soc.* **142**, 18042–18049 (2020).
12. M. Schleeger, C. C. Vandenakker, T. Deckert-Gaudig, V. Deckert, K. P. Velikov, G. Koenderink, M. Bonn, Amyloids: From molecular structure to mechanical properties. *Polymer* **54**, 2473–2488 (2013).
13. S. Abdelrahman, M. Alghrably, J. I. Lachowicz, A. H. Emwas, C. A. E. Hauser, M. Jaremko, "What doesn't kill you makes you stronger": Future applications of amyloid aggregates in biomedicine. *Molecules* **25**, 5245 (2020).
14. R. Virchow, Zur Cellulose—Frage. *Archiv f. pathol. Anat.* **6**, 416–426 (1854).
15. N. Friedreich, A. Kekulé, Zur Amyloidfrage. *Archiv f. pathol. Anat.* **16**, 50–65 (1859).
16. J. D. Sipe, A. S. Cohen, Review: History of the amyloid fibril. *J. Struct. Biol.* **130**, 88–98 (2000).
17. C. Dias, A. P. Rauter, Carbohydrates and glycomimetics in Alzheimer's disease therapeutics and diagnosis. *RSC Drug Discov. Ser.* **2015**, 180–208 (2015).
18. T. Bitter, H. Muir, Mucopolysaccharides of whole human spleens in generalized amyloidosis. *J. Clin. Investig.* **45**, 963–975 (1966).
19. J. H. Magnus, T. Stenstad, S. O. Kolset, I. M. Dahl, P. J. Ranløv, G. Husby, High molecular weight polysaccharides in familial cardiac amyloid of danish origin related to transthyretin met 111, in *Amyloid and Amyloidosis*, J. B. Natvig, Ed. (Springer, Dordrecht, 1991).
20. R. Bravo, M. Arimon, J. J. Valle-Delgado, R. García, N. Durany, S. Castel, M. Cruz, S. Ventura, X. Fernandez-Busquets, Sulfated polysaccharides promote the assembly of amyloid β1–42 peptide into stable fibrils of reduced cytotoxicity. *J. Biol. Chem.* **47**, 32471–32483 (2008).

21. D. J. Martin, M. Ramirez-Alvarado, Glycosaminoglycans promote fibril formation by amyloidogenic immunoglobulin light chains through a transient interaction. *Biophys. Chem.* **158**, 81–89 (2011).
22. M. Holubová, V. Lobaz, L. Loukotová, M. Rabyk, J. Hromádková, O. Trhlíková, Z. Pechrová, O. Groborz, P. Štěpánek, M. Hrubý, Does polysaccharide glycogen behave as a promoter of amyloid fibril formation at physiologically relevant concentrations? *Soft Matter* **17**, 1628–1641 (2021).
23. X. Zhan, B. Stamova, F. R. Sharp, Lipopolysaccharide associates with amyloid plaques, neurons and oligodendrocytes in alzheimer's disease brain: A review. *Front. Aging Neurosci.* **10**, 42 (2018).
24. J. W. Lee, Y. K. Lee, D. Y. Yuk, D. Y. Choi, S. B. Ban, K. W. Oh, J. T. Hong, Neuro-inflammation induced by lipopolysaccharide causes cognitive impairment through enhancement of beta-amyloid generation. *J. Neuroinflammation* **5**, 37 (2008).
25. F. G. Torres, O. P. Troncoso, A. Pisani, F. Gatto, G. Bardi, Natural polysaccharide nanomaterials: An overview of their immunological properties. *Int. J. Mol. Sci.* **20**, 5092 (2019).
26. Y. Habibi, L. A. Lucia, O. J. Rojas, Cellulose nanocrystals: Chemistry, self-assembly, and applications. *Chem. Rev.* **110**, 3479–3500 (2010).
27. P. Hassanzadeh, M. Kharaziha, M. Nikkhah, S. R. Shin, J. Jin, S. He, W. Sun, C. Zhong, M. R. Dokmeci, A. Khademhosseini, M. Rolandi, Chitin nanofiber micropatterned flexible substrates for tissue engineering. *J. Mater. Chem. B* **1**, 4217–4224 (2013).
28. Z. A. Arnon, M. Grabarics, T. Kreiser, A. Raveh, K. Pagel, E. Gazit, Inulin nanostructures: The sweet-spot of carbohydrate self-assembly. *bioRxiv* **13**, 451276 (2021).
29. J. P. Verbelen, S. Kerstens, Polarization confocal microscopy and Congo red fluorescence: A simple and rapid method to determine the mean cellulose fibril orientation in plants. *J. Microsc.* **198**, 101–107 (2000).
30. M. Biancalana, S. Koide, Molecular mechanism of Thioflavin-T binding to amyloid fibrils. *Biochim. Biophys. Acta.* **1804**, 1405–1412 (2010).
31. S. Shaham-Niv, P. Rehak, D. Zaguri, A. Levin, L. Adler-Abramovich, L. Vuković, P. Král, E. Gazit, Differential inhibition of metabolite amyloid formation by generic fibrillation-modifying polyphenols. *Commun. Chem.* **1**, 25 (2018).
32. I. Sirangelo, M. Borriello, G. Irace, C. Iannuzzi, Intrinsic blue-green fluorescence in amyloyd fibrils. *AIMS Biophys.* **5**, 155–165 (2018).
33. D. Zaguri, S. Shaham-Niv, P. Chakraborty, Z. Arnon, P. Makam, S. Bera, S. Rencus-Lazar, P. R. Stoddart, E. Gazit, N. P. Reynolds, Nanomechanical properties and phase behavior of phenylalanine amyloid ribbon assemblies and amorphous self-healing hydrogels. *ACS Appl. Mater. Interfaces* **12**, 21992–22001 (2020).
34. I. Rosales, L. Salazar, D. Luna, A. Negrón, I. Bdikin, B. J. Rodriguez, A. Heredia, I. Rosales, L. Salazar, D. Luna, A. Negrón, I. Bdikin, B. J. Rodriguez, A. Heredia, Self-assembly of amyloid-beta and its piezoelectric properties. *Am. J. Mol. Biol.* **11**, 1–14 (2020).
35. G. Ochbaum, R. Bitton, *Using Small-Angle X-Ray Scattering (Saxs) to Study the Structure of Self-Assembling Biomaterials* (Elsevier, Netherlands, 2018).
36. A. Singh, J. U. Joo, D. P. Kim, Microfluidic-driven ultrafast self-assembly of a dipeptide into stimuli-responsive 0D, 1D, and 2D nanostructures and as hydrolase mimic. *Nanoscale* **14**, 15010–15020 (2022).
37. F. J. Warren, M. J. Gidley, B. M. Flanagan, Infrared spectroscopy as a tool to characterise starch ordered structure—A joint FTIR–ATR, NMR, XRD and DSC study. *Carbohydr. Polym.* **139**, 35–42 (2016).
38. R. Zhao, M. So, H. Maat, N. J. Ray, F. Arisaka, Y. Goto, J. A. Carver, D. Hall, Measurement of amyloid formation by turbidity assay—Seeing through the cloud. *Biophys. Rev.* **8**, 445–471 (2016).
39. U. N. Morzan, G. Díaz Mirón, L. Grisanti, M. C. González Lebrero, G. S. Kaminski Schierle, A. Hassanali, Non-aromatic fluorescence in biological matter: The exception or the rule? *J. Phys. Chem. B* **126**, 7203–7211 (2022).
40. S. Gilead, E. Gazit, The role of the 14-20 domain of the islet amyloid polypeptide in amyloid formation. *Exp. Diabetes Res.* **2008**, 256954 (2008).
41. A. Singh, J. P. Joseph, D. Gupta, I. Sarkar, A. Pal, Pathway driven self-assembly and living supramolecular polymerization in an amyloid-inspired peptide amphiphile. *Chem. Commun.* **54**, 10730–10733 (2018).
42. L. Adler-Abramovich, L. Vaks, O. Carny, D. Trudler, A. Magno, A. Caflisch, D. Frenkel, E. Gazit, Phenylalanine assembly into toxic fibrils suggests amyloid etiology in phenylketonuria. *Nat. Chem. Biol.* **8**, 701–706 (2012).
43. I. Usov, R. Mezzenga, FiberApp: An open-source software for tracking and analyzing polymers, filaments, biomacromolecules, and fibrous objects. *Macromolecules* **48**, 1269–1280 (2015).
44. H. W. Wang, H. W. Zhou, L. L. Gui, H. W. Ji, X. C. Zhang, Analysis of effect of fiber orientation on Young's modulus for unidirectional fiber reinforced composites. *Compos. B Eng.* **56**, 733–739 (2014).
45. S. Bolisetty, J. J. Vallooran, J. Adamcik, R. Mezzenga, Magnetic-responsive hybrids of Fe_3O_4 nanoparticles with β-lactoglobulin amyloid fibrils and nanoclusters. *ACS Nano* **7**, 6146–6155 (2013).
46. I. Usov, J. Adamcik, R. Mezzenga, Polymorphism complexity and handedness inversion in serum albumin amyloid fibrils. *ACS Nano* **7**, 10465–10474 (2013).
47. K. Xu, W. Sun, Y. Shao, F. Wei, X. Zhang, W. Wang, P. Li, Recent development of PeakForce Tapping mode atomic force microscopy and its applications on nanoscience. *Nanotechnol. Rev.* **7**, 605–621 (2018).
48. A. H. Tayeb, E. Amini, S. Ghasemi, M. Tajvidi, Cellulose nanomaterials—Binding properties and applications: A review. *Molecules* **10**, 2684 (2018).
49. V. Basavalingappa, S. Bera, B. Xue, J. O'donnell, S. Guerin, P.-A. Cazade, H. Yuan, U. Haq, C. Silien, K. Tao, L. J. W. Shimon, S. A. M. Tofail, D. Thompson, S. Kolusheva, R. Yang, Y. Cao, E. Gazit, Diphenylalanine-derivative peptide assemblies with increased aromaticity exhibit metal-like rigidity and high piezoelectricity. *ACS Nano* **14**, 7025–7037 (2020).
50. P. Makam, S. S. R. K. C. Yamijala, K. Tao, L. J. W. Shimon, D. S. Eisenberg, M. R. Sawaya, B. M. Wong, E. Gazit, Non-proteinaceous hydrolase comprised of a phenylalanine metallo-supramolecular amyloid-like structure. *Nat. Catal.* **2**, 977–985 (2019).
51. D. Otzen, R. Riek, Functional amyloids. *Cold Spring Harb. Perspect. Biol.* **11**, a033860 (2019).
52. Y. Chen, A. A. Orr, K. Tao, Z. Wang, A. Ruggiero, L. J. W. Shimon, L. Schnaider, A. Goodall, S. Rencus-Lazar, S. Gilead, I. Slutsky, P. Tamamis, Z. Tan, E. Gazit, High-efficiency fluorescence through bioinspired supramolecular self-assembly. *ACS Nano* **14**, 2798–2807 (2020).
53. H. Xiang, Z. Li, H. Liu, T. Chen, H. Zhou, W. Huang, Green flexible electronics based on starch. *NPJ Flex. Electron.* **6**, 15 (2022).
54. I. Cherny, E. Gazit, Amyloids: Not only pathological agents but also ordered nanomaterials. *Angew. Chem. Int. Ed. Engl.* **47**, 4062–4069 (2008).
55. S. Bera, S. Mondal, B. Xue, L. J. W. Shimon, Y. Cao, E. Gazit, Rigid helical-like assemblies from a self-aggregating tripeptide. *Nat. Mater.* **18**, 503–509 (2019).
56. S. Wei, Y. Li, K. Li, C. Zhong, Biofilm-inspired amyloid-polysaccharide composite materials. *Appl. Mater. Today* **27**, 101497 (2022).
57. G. Tan, L. Wang, W. Pan, K. Chen, Polysaccharide electrospun nanofibers for wound healing applications. *Int. J. Nanomedicine* **17**, 3913 (2022).
58. B. Farasati Far, M. R. Naimi-Jamal, M. Safaei, K. Zarei, M. Moradi, H. Yazdani Nezhad, A review on biomedical application of polysaccharide-based hydrogels with a focus on drug delivery systems. *Polymers* **24**, 5432 (2022).

Acknowledgments: We thank R. Mezzenga for providing free access to MATLAB, FiberApp application that was used for the analysis of morphology of the fibrils. We extend our thanks to Bruker USA for the assistance in mechanical stiffness calculations. In addition, we acknowledge the assistance provided by R. Gross, S. Pryshchep, and N. Dhull, Rensselaer Polytechnic Institute, New York, in the AFM stiffness studies. **Funding:** We extensively thank ISF Research grant no. 1558/19 for funding support. S.C. thanks the Tel Aviv University for the fellowship and financial assistance. **Author contributions:** Writing original draft: E.G., S.C., and A.S. Investigation: S.C., A.S., G.F.-Z., and R.B. Validation: S.C., A.S., and E.G. Formal analysis: S.C., A.S., and G.F.-Z. Methodology: S.C., A.S., G.F.-Z., G.K., and E.G. Software: A.S. and S.C. Writing–reviewing and editing: S.R.-L. and E.G. Resources: R.S. and E.G. Conceptualization: E.G. Funding acquisition: E.G. Data curation: E.G. Supervision: E.G. Project administration: E.G. Visualization: E.G. **Competing interests:** The authors declare that they have no competing interests. **Data and materials availability:** All data needed to evaluate the conclusions in the paper are present in the paper and in the Supplementary Materials.

Submitted 4 April 2024
Accepted 25 July 2024
Published 30 August 2024
10.1126/sciadv.adp6471